Check for updates

High output achieved by sliding electrification of an electrospun nano-grating†

Li-Na Zhou,‡[a] Jun-Peng Wu,‡[a] Wei-Zhi Song,[a] Xiao-Xiong Wang,[a] Ning Wang,[a] Miao Yu,[a] Zhi-Yong Fan, [ID][b] Seeram Ramakrishna [ID][c] and Yun-Ze Long [ID] *[a,d]

The rapid development of flexible and wearable electronics has proposed a trend towards miniaturization, mobility, versatility and artificial intelligence. Triboelectric nanogenerators (TENGs) can make use of micro/nano multi-functional materials to harvest and store energy from the surrounding environment efficiently, which can drive smart portable electronics operating continuously and steadily. The increase in the output power density of the triboelectric nanogenerator requires new designs. In this work, a new grating TENG was proposed, and the two friction layers were fabricated by near-field electrospinning and conventional electrospinning with two parallel electrodes as a collector, respectively. The basic model of the simulation was simplified according to the highly ordered structure and the repeatability of the TENG grating structure. The effect of the effective contact area on the output of the TENG was further proved by fitting the calculation regularity of the two models with the experimental results. At the same time, the effect of the redundant electrode on the output of the TENG was verified by experiments. We found that this nanogenerator can achieve a very high output of 1800 W m^{-2} due to a more refined grating structure combined with modification of the contact area. The TENG can also be used as a selfpowered sensor to detect mechanical signals, which requires no additional power source to drive it. Meanwhile, the anisotropic nature of the TENG can also be utilized to sense angles, lock devices or encrypt information. This output control technology provides a more effective idea for future output power improvement, that is, a new generation of high-output TENGs can be designed by effectively adjusting the corresponding contact area and electrode area.

1. Introduction

After the rapid development of portable and wearable wireless devices over the past decade, people are now focusing more on novel entirely self-powered electronic devices and electronic systems.[1–3] The invention of triboelectric nanogenerators (TENGs) was a milestone in the field of mechanical power generation and self-powered systems.[4] This provides a completely new model for efficient collection of mechanical energy (whether organic or inorganic).[5,6] TENGs can be used to collect all kinds of mechanical energy that is being wasted, including energy generated by human activities,[7] mechanical triggering,[8–14] and tire rotation,[15] wind energy,[16] water energy[17–20] and many other forms of energy. TENGs can also be used as self-powered sensors to detect mechanical signals. The open circuit voltage can be used for static measurement,[21,22] such as alarms, temperature sensors,[23] light sensors, *etc.*, while short-circuit current signals can be used for dynamic measurements,[24,25] such as breath detection.

Through lithography, etching or self-assembly construction, structures such as lines, cubes or pyramids can be formed to control the surface roughness, thereby enhancing the output of the nanogenerator.[26,27] However, these technologies are often expensive and have limited application. Electrospinning is a method for the direct and continuous preparation of polymer nanofibers, and can produce scalable TENGs.[28,29] Conventional electrospinning produces disordered rough surfaces. However, oriented fiber membranes can be obtained by changing the receiving device,[30–34] controlling the electric field,[35–37] or adding a magnetic field.[38] For example, near-field electrospinning (NFES)[39,40] can be used to prepare individual fibers and for fiber patterning, while ordered nanofibers can be produced using parallel electrodes[41] or high-speed rollers.[42]

[a]*Collaborative Innovation Center for Nanomaterials & Devices, College of Physics, Qingdao University, Qingdao 266071, China. E-mail: yunze.long@163.com, yunze.long@qdu.edu.cn; Tel: +86 139 5329 0681*
[b]*Department of Electronic & Computer Engineering, The Hong Kong University of Science & Technology, Kowloon, Hong Kong, China*
[c]*Center for Nanofibers & Nanotechnology, Department of Mechanical Engineering, National University of Singapore, Singapore 117574*
[d]*Collaborative Innovation Center for Eco-Textiles of Shandong Province, and State Key Laboratory of Bio-Fibers & Eco-Textiles, Qingdao University, Qingdao 266071, China*
†Electronic supplementary information (ESI) available. See DOI: 10.1039/d1nr04769h
‡These two authors contributed equally to this work.

The ordered alignment morphology will improve the mechanical properties of the fiber significantly,[43] and provide a new approach of controlling the roughness.

In this work, a TENG was prepared using polyvinylidene fluoride (PVDF) prepared by near-field electrospinning and nylon 6 (PA6) prepared by parallel electrode collection technology. Compared with the previously reported micro-grating,[44] the fiber arrays formed a more precise grating topography, achieving a high output. The output performance of this grating TENG is systematically studied, especially the influence of pressure and electrode area changes on its output performance. This TENG is demonstrated to be capable of powering a variety of devices. More importantly, this grating TENG has anisotropic output performance, which can be used for safety applications such as password locks or encrypted communication.

2. Experimental section

2.1 Materials

Polyvinylidene fluoride (PVDF) powder (M_w ~1 000 000) and nylon 6 (PA6) powder were purchased from Macklin Biochemical Co., Ltd, China. N,N-Dimethylformamide (DMF), 88% strength formic acid, acetic acid and ethanol were supplied by Sinopharm Chemical Reagent Co., Ltd, China. Acetone was supplied by Laiyang Fine Chemical Factory, China. All reagents were used as received.

2.2. Fabrication of the TENG

First, PVDF powder was dissolved in a DMF–acetone solvent mixture, and then stirred at 40 °C in a water bath for 6 h. To prepare a 20 wt% PA6 solution, PA6 pellets were dissolved in formic acid–acetic acid (1/1 w/w) and stirred continuously for 6 h at room temperature.

First, aluminum foil was fixed on a two-dimensional (2D) moving platform, and a needle tube was fixed directly above the aluminum foil through the iron frame, and the spinning voltage was 3.2 kV. The program parameters of the two-dimensional (2D) moving platform were the movement rate of the Y axis: 450 mm s^{-1}, the acceleration of the Y axis: 450 mm s^{-2}, the movement rate of the X axis: 0.1 mm s^{-1}, the acceleration of the X axis: 80 mm s^{-2}, and the repetition period was 800 times. The speed of the syringe pump during the electrospinning of PVDF was 1 µl min^{-1}, the volume of the syringe was 2.5 ml, the spinning distance was 1 cm, the inner diameter of the needle was 0.26 mm, and the temperature was 28 ± 3 °C. The atmospheric humidity was 38 ± 5%. The collection station movement was then controlled by a 2D programmable platform. The main role of near-field electrospinning was to achieve controlled deposition of fibers. The charged jets were ejected from the spinning head under the action of a high-voltage electrostatic field. The initial stage moves along a linear path to form an ordered fiber structure.

First, two Al foil sheets of the same size were placed on a receiving plate, and Al foil paper was attached to the negative electrode of the power source, respectively, and the gap between the two Al foil sheets was 3 cm. A needle was then fixed directly above the gap using an iron stand. The speed of the syringe pump during the electrospinning of PA6 was 0.5 ml h^{-1}, the inner diameter of the needle was 0.51 mm, and the volume of the syringe was 2.5 ml. During the electrospinning process, the ordered fiber membrane of PA6 was prepared at a voltage of 16 kV, a rotation distance of 15 cm, a temperature of 26 ± 3 °C and a humidity of 32 ± 5%. The fiber was straightened and deposited in a direction perpendicular to the electrode because of an electrostatic force generated during the falling process and the fiber was finally collected between the two electrodes.

2.3. Characterization and measurements

The surface morphology and microstructure of the TENG were investigated by scanning electron microscopy (SEM, TM-1000, Hitachi). The current output of the TENG was tested using a current amplifier (SR570), a picoammeter (Keithley 6487) and a digital oscilloscope (GDS-2102, Gwinstek). The digital oscilloscope (GDS-2102, Gwinstek) records the voltage signal of the TENG. The charging test of commercial capacitors was performed using a digital multimeter (Rigol DM 3058). Near-field electrostatic spinning was carried out using an X–Y axis precision mobile platform, which was composed of a servo motor (Japan Yaskawa SGDV-R70F01A00200), a sensor (Japan Omron E2B-S08KN02), and a controller (Crt DMC630M). The generation of TENG periodic signals was investigated using a self-made device. The schematic and working principle of the device are shown in Fig. S1.†

3. Results and discussion

3.1 Basic character of the grating TENG

The triboelectric effect is a charging effect caused by contact, that is, charge transfer occurs during the friction process of one material with another material. The polarity of the charge carried by a material depends on the relative polarity of the contact material.[45,46] A PVDF ordered fiber membrane was prepared using a near-field electrospinning apparatus. The schematic is shown in Fig. 1a. A schematic diagram of the preparation process of the ordered structure of the PA6 membrane is shown in Fig. 1b. The TENG consists of two aluminum electrodes with a friction layer of PVDF and PA6, respectively. According to the symmetry demonstration, the simplified TENG model is shown in Fig. 1c. The working principle of the TENG is shown in Fig. 1d. In the initial state (i), the PVDF membrane was in contact with the PA6 membrane and no current or potential appears. Due to the difference in the surface electron affinity, charge will transfer from the surface of the PA6 membrane to the surface of the PVDF membrane, leaving a net positive charge on the surface of the PA6 nanofibers and a net negative charge on the surface of the PVDF nanofibers. When separated, if the device was connected to an external circuit, the final charge separation creates a potential difference (state ii) on the contact surface, causing subsequent current flow. At the maximum spacing, the positive open
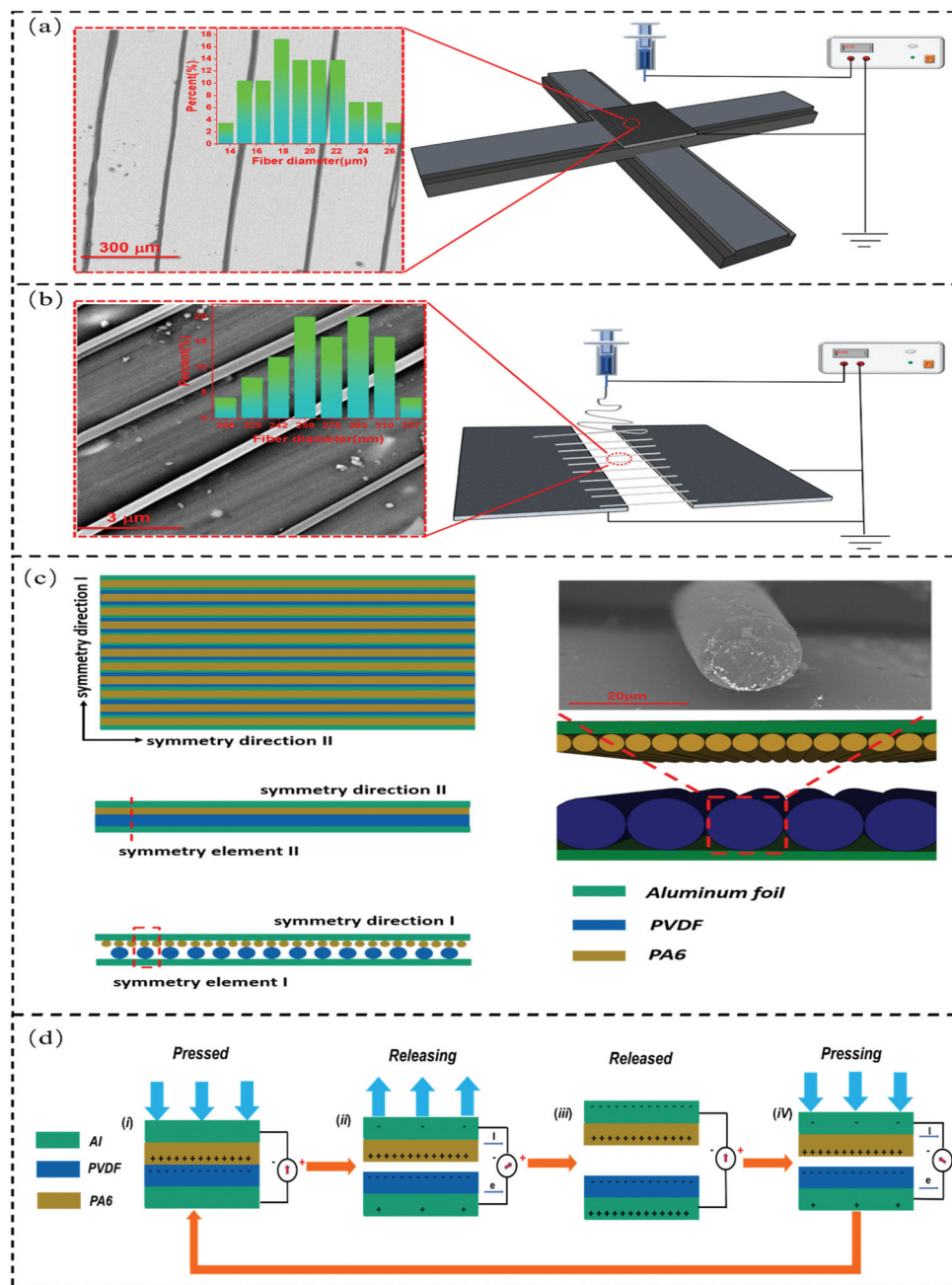
Fig. 1 (a) Preparation process of PVDF oriented fibers by near-field electrospinning and the SEM image of oriented PVDF fibers. (b) SEM image of PA6 fibers and oriented PA6 fibers prepared by the electrospinning process obtained using parallel plates. (c) A schematic diagram of the simplified TENG model, including a top view, a side view, and a cross-sectional view, as well as a fiber cross-sectional view of PVDF. (d) Schematic diagram of the contact-separated generator of the TENG of this work.

circuit was reduced to zero (state iii). When the two charged surfaces were in contact again, the current was reversed (state iv), without any contact, no charge was transferred.

The output performance of the TENG was systematically investigated. The ordered structure of the electrospun fibers effectively increases the specific surface area of the contact, making it easier for PVDF fiber membranes and PA6 fiber membranes to gain or lose electrons during contact. The performance of the grating TENG was tested under different oper-

ating conditions. The gap distance between the triboelectric layers and the effects of frequency and humidity on the TENG have also been explored. The output performance of the TENG at a 2 Hz impact frequency for 3600 s is shown in Fig. 2a and b. The comparison of the morphologies of PVDF fibers and PA6 fibers before and after cycling is shown in the Fig. S2.† The morphology of PVDF fibers did not change significantly before and after the cycle, and the PA6 fibers accumulated. The magnitudes of the current and voltage were 870 nA and
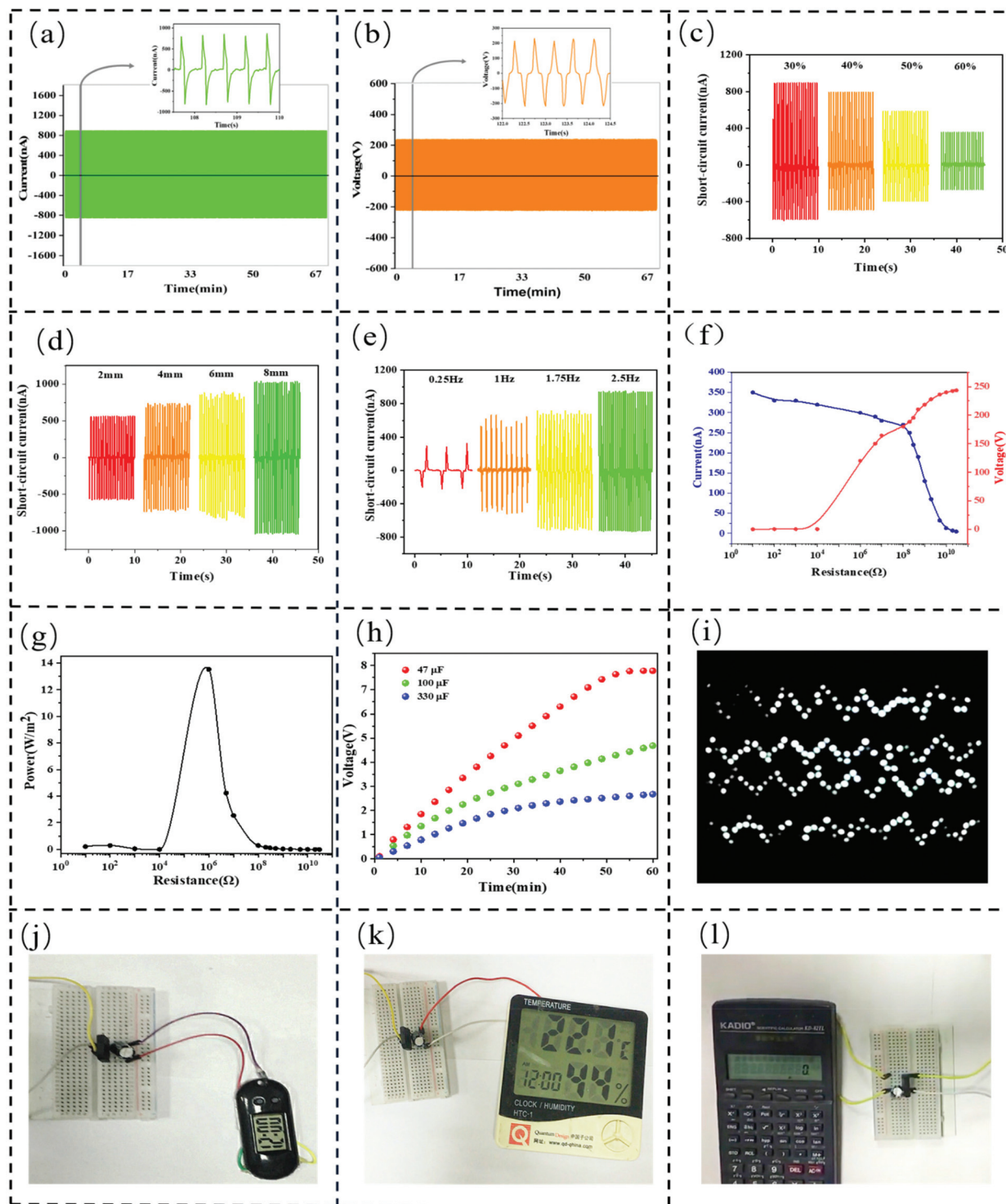
Fig. 2 TENG stability and durability testing. (a) Cyclic current signal and short-term current signal of the TENG. (b) Cyclic current signal and short-term current signal of the TENG voltage. Electrical performance of the TENG. (c) Short-circuit current of the TENG under 2 Hz frequency impact at different atmospheric humidities. (d) Short-circuit current of the TENG under 2 Hz frequency impact at different gap distances between the triboelectric layers. (e) Short-circuit current of the TENG with different impact frequencies. (f) Output current and voltage of the TENG with variation of load resistance. (g) Output power dependence on load resistance. (h) Charging curve of different commercial capacitors by the grating TENG. (i) The grating TENG can illuminate 230 LEDs without the need for an additional storage power unit. The TENG can drive many electronic devices to work properly such as (j) electronic watches, (k) temperature and humidity sensors, and (l) calculators.

228 V without obvious decay over time. Fig. 2c shows that the effect of humidity on the nanogenerator was particularly obvious. As the humidity increases, the current output of the TENG decreases significantly. Fig. 2d shows that the short-circuit current of the TENG increases gradually as the distance between the friction layers increases (details can be found in Fig. S3†). Fig. 2e shows that as the impact frequency increases, the short-circuit current of the TENG also increases. A higher impact frequency reduces the duration of the current peak and increases the amount of short-circuit current. The relationship between the load resistance and the electrical output signal was also tested systematically. It can be seen from Fig. 2f that according to the power formula $P = \frac{U^2}{R}$, the voltage and resistance were positively correlated, and the current and resistance were inversely correlated. The power curve obtained is shown in Fig. 2g, with an external load resistance of 4.9 MΩ and a maximum power density of 13.5 W m^{-2}. The relative load voltage and current can reach 97.3 V and 300 nA, respectively. Fig. 2h shows the plot of 47 μF, 100 μF and 330 μF commercial capacitors charging at a 2 Hz impact frequency.

The TENG with a contact area of 2×6 cm^2 provides a continuous and stable electrical signal output. As shown in Fig. 2h, a 47 μF commercial capacitor can be charged to 7.8 V at an operating frequency of 2 Hz. The stored energy can power a small portable smart electronic device. Properly designed self-powered systems can get rid of environmentally harmful batteries and improve the flexibility of electronic systems. The TENG with excellent stability was a high-quality energy supply that can power a variety of different forms of electronic equipment. Visual demonstrations were performed using an ordered structure of the TENG with a contact area of 2×6 cm^2. As shown in Fig. 2i and Video S1,† the ordered structure of the TENG can directly illuminate 230 white LEDs. In addition, the grating TENG can drive a variety of small electronic devices, such as temperature and humidity sensors, calculators and electronic meters, by charging 100 μF commercial capacitors to 4.7 V. The demonstration of the operations shown in Fig. 2j–l are shown in Videos S2–S4.† It can be seen that the ordered structure of the TENG exhibits good energy harvesting capability and has great development potential in the field of portable devices, which was beneficial for the promotion of the ordered structure of the TENG.

3.2 Output analysis of the grating TENG

The actual contact area of the TENG was different under different contact forces, while the model of Dharmasena et al.,[47] the model of Shao et al.,[48] and the model of Wang et al.[49] mainly focus on the macroscopic contact area of the TENG, not the actual contact area of the TENG. It was impossible to predict the change of the actual contact area and output performance of the TENG under different forces. Therefore, we choose a first-order lumped-parameter equivalent circuit model (FLEC model) and a load-dependent model to predict the output performance of the TENG under different contact forces.

In the load-dependent model, COMSOL simulation (version 5.4, the detailed simulation parameters can be found in the

ESI†) was used to solve the actual contact area related to the load. The arrangement of fibers makes the analysis of related properties easier. In the film plane perpendicular to the fiber direction, it can be approximated that the TENG was obtained by the translation of periodic PVDF and PA6 fiber contact pairs, so the final contact pair of one PVDF fiber and one PA6 fiber can represent the contact and electrification of the entire film. For remaining PA6 fibers which cannot contact PVDF, they do not participate in the electrification process and do not contribute to the electrification process. In the direction along the fiber, a pair of fibers can be obtained by translating the cross section. For a single fiber, its cross-section is approximately circular, as shown in the SEM image in Fig. 1c. Then the electrode-PVDF fiber-PA6 fiber-electrode cross section was used to simulate the entire electrification state of the membrane. When pressure is applied to the fiber, the contact surface area of the two fibers changes. Fig. 3a shows the pressure distribution on the fiber contact surface under a certain degree of compression. Fig. 3b shows that as the pressure continues to increase, the contact area between the fibers also increases.

The first-order lumped-parameter equivalent circuit model (FLEC model) by Niu et al.[50] was considered. The basic structure of the model is shown in Fig. S4.† r_1 and r_2 are the thickness of the PVDF fiber and PA6 fiber respectively, εr_1 and εr_2 are the relative permitivities, σ is the charge density, and S is the electrode area. The sum of the thickness of all dielectric materials between the two electrodes and the value of their relative permittivity was defined as r_0:

$$r_0 = \sum_{i=1}^{n} \frac{r_i}{\varepsilon_{ri}} \tag{1}$$

$$R\frac{dQ}{dt} = V = -\frac{1}{C}Q + V_{oc} \tag{2}$$

For any initial boundary conditions, the output of the TENG will gradually become a periodic output after a few cycles. The steady-state output of this periodic motion excitation was used when $Q (t = 0) = 0$. Under the boundary conditions, the current was:

$$I(t) = \frac{V_{oc}}{R} - \frac{1}{R^2 C} \exp\left[-\frac{1}{R}\int_0^t \frac{1}{C(x(t))}dt\right] \int_0^t V_{oc}(x(t)) \exp\left[\frac{1}{R}\int_0^t \frac{1}{Cx(t)}dt\right] \tag{3}$$

Simplified to:

$$I(t) = \frac{\sigma r_0}{R\varepsilon_0} + \frac{\sigma(r_0 + x(t))}{R\varepsilon_0} \exp\left[-\frac{1}{RS\varepsilon_0}\left(r_0 t + \int_0^t X(t)dt\right)\right]$$
$$+ \frac{\sigma r_0}{R\varepsilon_0} \times \frac{r_0 + x(t)}{R\varepsilon_0} \exp\left[-\frac{1}{RS\varepsilon_0}\left(r_0 t + \int_0^t x(t)dt\right)\right]$$
$$\times \int_0^t \exp\left[\frac{1}{RS\varepsilon_0}\left(r_0 z + \int_0^t x(z)dz\right)\right]dz \tag{4}$$

In the special case, from the time when the fiber starts to contact $x (t = 0) = 0$ to the maximum distance
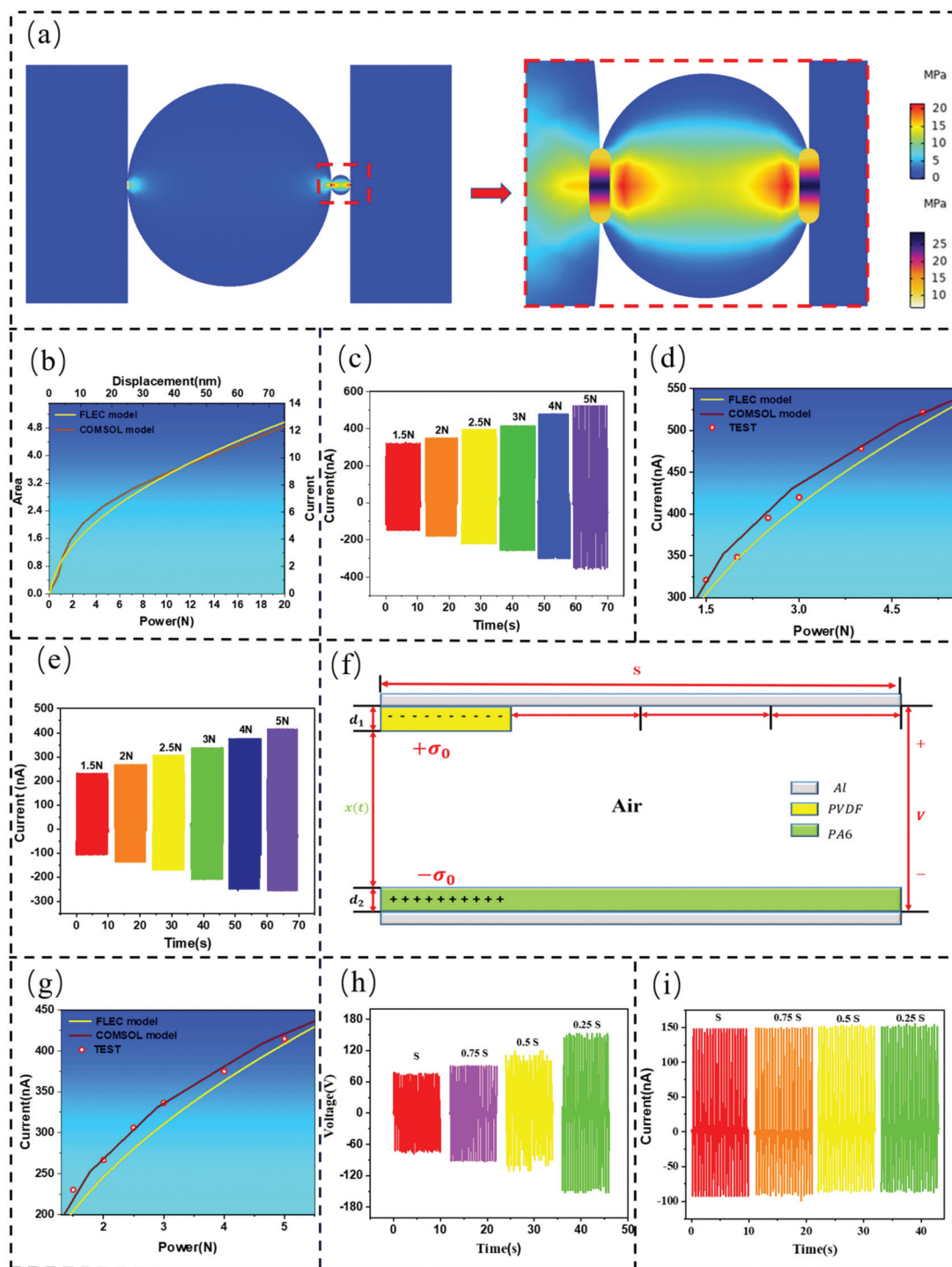
Fig. 3 (a) COMSOL simulates the pressure distribution during the compression of PVDF and PA6 fibers. (b) A FLEC model and a load-dependent model predict the output of the TENG with a gating structure at different contact forces. (c) Current output of the grating TENG under different pressures. (d) The current output of the grating TENG and the fitting result of the load-dependent curve and the FLEC curve. (e) Current output of the traditional unordered TENG under different pressures. (f) The equivalent circuit diagram of the TENG. (g) The current output of a general TENG and the fitting result of the load-dependent curve and the FLEC curve. (h) Voltage output under different electrode areas. (i) Current output under different electrode areas.

$x_{\max}$ when the fiber was compressed, it was a uniform motion:

$$x = vt\left(t \leq \frac{x_{\max}}{v}\right) \tag{5}$$

$$I(t) = \sigma s\Big[\exp(-At - Bt^2(A + 2Bt) - \sqrt{2}F \exp$$
$$(-At - Bt^2)(A + 2Bt) \times \mathrm{Dawson}\left(\frac{F}{\sqrt{2}}\right) - A + 2A \tag{6}$$
$$\left(\frac{F}{\sqrt{2}} + \sqrt{B}t\right) \times \mathrm{Dawson}\left(\frac{F}{\sqrt{2}} + \sqrt{B}t\right)\Big]$$

$$A = \frac{r_0}{RS\varepsilon_0} \tag{7}$$

$$B = \frac{v}{2RS\varepsilon_0} \tag{8}$$

$$F = \frac{A}{\sqrt{B}} = \frac{r_0}{\sqrt{2RS\varepsilon_0}} \tag{9}$$

$$S = 2r_1\Delta x - \Delta x^2 \quad (\Delta x = x_{t_2} - x_{t_2}, 0 \leq t_1, t_2 \leq t) \tag{10}$$

The Dawson function definition is

$$\mathrm{Dawson}(x) = \exp(-x^2)\int_0^x \exp(y^2)\mathrm{d}y \tag{11}$$

In eqn (2), the internal resistance of the TENG is R, the voltage of the external circuit is V, the capacitance between the TENG electrodes is C, and the open circuit voltage of the TENG is V_{oc}. In eqn (5), v is the separation velocity of the friction layer. In eqn (10), Δx represents the displacement difference.

Therefore, the output result of the FLEC model was the curve in Fig. 3b.

In order to verify whether the law given by the two model analysis was consistent with the actual situation, the output of the grating TENG under different pressures was also tested. The output pressure was controlled by the design of spring constraints. The stiffness coefficient K of the spring was 8 g mm^{-1}. The output current was measured when the spring compression was 0.18 mm, 0.25 mm, 0.32 mm, 0.38 mm, 0.5 mm and 0.62 mm, respectively. The length of the spring constraint determines the magnitude of the pressing force after contact, and this force was determined by Hooke's law. The results are shown in Fig. S5.† In the figure, it can be seen that as the force increases, the effective contact area increases, the amount of charge Q on the friction layer surface increases, the external circuit current increases, and σ increases.

The results are shown in Fig. 3c, in the case of controlling the only variable pressure, the greater the pressure, the stronger the current output. The regularity of the FLEC models shown in Fig. 3b and the output tendency shown in Fig. 3c can be matched with each other. However, the simulation model of load-dependent fits better with the output trend shown in Fig. 3c, and the matching results are shown in Fig. 3d. In the ordered TENG, as the pressure increases, the effective contact area between the fibers increases, so the TENG current output becomes larger. This trend was similar to the regulation reported in other disordered structures.[51] In order to further verify the

effectiveness of the load-dependent model, the regularity of the two models was matched with the output trend of the disordered TENG. So the friction layers of the disordered PVDF membrane and the PA6 membrane were also tested. The SEM images of the PVDF membrane and the PA6 membrane are presented in Fig. S6.† The systematic investigation shows that the trend was consistent with the ordered ones, it was also found that the regularity of the load-dependent model was more in line with the experimental results, which may be attributed to the similar sectional shape, and the current output under different pressures is shown in Fig. 3e. With the increase of pressure, the current continues to increase, as shown in Fig. 3g.

The existence of the redundant electrode area was limited by the fabrication technique, that is to say, the fibers require support from the electrode. The decrease of the electrode area will increase the output voltage due to the decrease of capacitance, and the output will be further increased. So if the redundant electrode can be removed by a future technique, a larger output power density will be achieved. Here the TENG (length 80 mm, width 20 mm) with disordered fibers was used to verify the influence of electrode area changes on the electrical signal output. The experimental configuration is shown in Fig. 3f. The electrode area of the TENG was S, the area of PVDF was 1/4 S, and the area of PA6 was equal to the electrode area. After reducing the electrode area from S to smaller ones, the current and voltage were measured. The experimental results are shown in Fig. 3h and i. As the electrode area decreases, the voltage output of the TENG continues to increase, but the current output does not change significantly. This phenomenon was in agreement with the known theory commonly used in the area of nanogenerators, as discussed below.

The basic structure of the TENG is shown in Fig. 3f. PVDF and PA6 were effective friction layers with thicknesses d_1 and d_2, relative permittivities ε_{r1} and ε_{r2}, charge density σ, and electrode area S. The sum of the thickness of all dielectric materials between the two electrodes and the value of their relative permittivity was defined as d_0:

$$d_0 = \sum_{i=1}^{n} \frac{d_i}{\varepsilon_{ri}} \tag{12}$$

The induced potential difference was V, the amount of charge transfer was Q, and the TENG's V–Q–x relationship was defined as:

$$V = -\frac{Q}{S\varepsilon_0}(d_0 + x(t)) + \frac{\sigma x(t)}{\varepsilon_0} \tag{13}$$

Derived from the electrodynamics open circuit output voltage V_{oc} and output charge Q_{sc}:

$$V_{oc} = \frac{\sigma x(t)}{\varepsilon_0} \tag{14}$$

$$Q_{sc} = \frac{S\sigma x(t)}{d_0 + x(t)} \tag{15}$$

Take the node $x = x(t)$ for discussion, when the electrode area is reduced, for the entire capacitor structure, the friction

area remains unchanged, the surface charge density σ_0 remains unchanged, and the charge transfer amount Q remains unchanged:

$$Q = S\sigma_0 \tag{16}$$

$$Q_{sc} = \frac{S\sigma x}{d_0 + x} \tag{17}$$

$$V_{oc} = \frac{\sigma x}{\varepsilon_0} \tag{18}$$

$$Q_{sc} = \int I \mathrm{d}t \tag{19}$$

Since $Q_{sc} = Q$, the electrode area S decreases continuously, Q_{sc} does not change, the charge density σ on the electrode surface gradually increases, the dielectric constant ε_0 does not change, and the open circuit voltage V_{oc} increases continuously, which was consistent with the experimental results in Fig. 3h. Since Q_{sc} does not change, according to the current integral formula, the current output does not change when the cycle was stable, which conforms to experimental results in Fig. 3i.

In the actual friction process of the TENG, as shown in Fig. S5f,† S not all the contact of the membrane was the effective contact area, only a few areas were effectively contacted, and the electrodes outside the effective contact area were redundant electrodes. The contact area between the PA6 fiber and the PVDF fiber was the effective contact area. Without considering the redundant electrodes, the output power of the TENG can reach 1800 W m^{-2}, and the surface charge density can reach 5.09 C m^{-2} (details can be found in Fig. S5 and S7S†). In order to increase the output power of the TENG prepared by electrospinning, an effective way was proposed (details are given in Table S1†).

3.3 Anisotropy of the grating TENG

For the grating TENG, the output can be effectively affected by the micro contact situation, so a change in the relative angle of the fiber will cause a change of the output current/voltage (details can be found in Fig. S8†). Hence, the output variation of the grating TENG was explored after changing the relative direction of the two layers. First, in order to ensure that the contact area does not change with the angle, two circular Al foils with a radius of 2.2 cm were used as electrodes, and the ordered PVDF and PA6 structures were electrospun on the Al foil as described above, as shown in Fig. 4a. Then the output current was tested for different relative angles at a fixed impact frequency of 2 Hz. As shown in Fig. 4b, we fit multiple sets of current peaks at the same angle, as shown in Fig. 4c. When the two sets of fiber arrays were aligned, there will be a maximum output. If the relative angle changes then, the output will decrease. The peak current has a linear relationship with the relative angle. Therefore, the relative angle change between two objects can be characterized by the peak current, so it can be used as a self-powered angle sensor.

Meanwhile, the peak current at different angles demonstrated good repeatability.

Based on the anisotropy and stability of the ordered structure, a self-powered ternary lock structure was designed. As shown in Fig. S9a,† the bottom of the device was a 5 × 5 cm^2 plate clamp, placed on the plate with a 4 × 4 cm^2 sponge layer, and a 2 cm radius of PA6 fiber aluminum foil placed on the sponge. The iron posts and springs on the device act to limit and reset. In order to ensure a certain pressure, a limit log was placed around the spring. An aluminum foil disc with a radius of 2 cm was placed under the 5 × 5 cm^2 plate above the device, and the Al foil disc was spun with an ordered structure of PVDF. Holes were punched in the upper plate for simple 45° and 90° rotations. Subsequently, the relative parallel state of the two fibers was set to 0°, and measurements were performed at 45° and 90° rotation angles, respectively, and current tests on these three states were performed. As shown in Fig. S9b–d,† the 0°, 45° and 90° current output signals were in a manual pressed state. The current signal has good stability, and the current difference of the three states was more obvious.

Electronic code locks are widely used in daily life. The electronic code lock is an electronic product that controls the circuit or chip operation (access control system) through password input, thereby controlling the closing of the mechanical switch and completing the unlocking and locking tasks. Most of the electronic code lock structures require a constant supply of energy, which causes a waste of some energy. By referring to the output of the grating TENG in states when the two layers are in three different relative angles, a self-powered ternary electronic code lock structure was designed. A demonstrative electronic code lock consisting of three grating TENGs can be used to set a password. If the current output of 0° was defined as 0, the current output of 45° was defined as 1, and the current output of 90° was defined as 2, each TENG has three kinds of output signals, then there are totally 27 combined signal outputs. This device can also be used to encrypt information. If the 26 English characters are encoded from 001 to 222, the information will be encrypted. As shown in Fig. S10,† if the code was written as QDU, then "Q" is 122, "D" is 011, and "U" is 210, and for those who do not know the anisotropy setting, they will get wrong information.

Based on the anisotropy, an anti-counterfeiting device can be designed. As shown in Fig. 4e, the macroscopically observed pattern was "8", but this was fake information. In fact, the 7 areas on the number "8" are respectively represented as a–g. The ordered fibers in the f area are arranged horizontally, and the fibers in other positions were arranged vertically. This design rubs against PA6 as a whole, and the area f will produce a different output, as the output current of vertical friction and parallel friction was significantly different, so that the real data are 9 instead of 8. If the current signal generated by 90° friction was defined as the effective signal, and 0° was ineffective, different camouflaged numbers can be coded. As shown in Fig. 4e, if the two friction angles in the b and f areas are set to 0°, and the friction angles of other areas are set to 90°, then
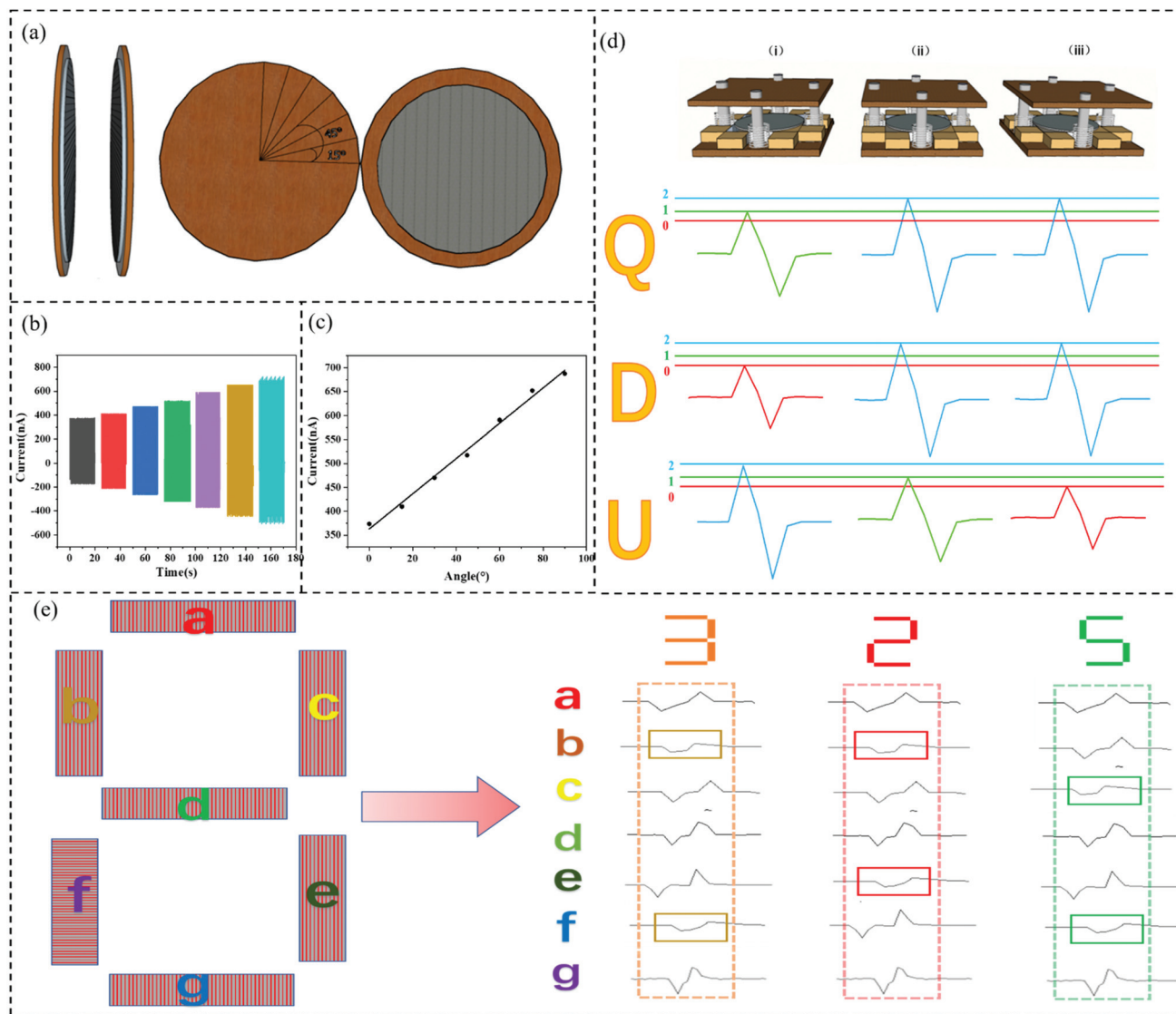
Fig. 4 (a) Schematic diagram of the device structure. (b) Current at different angles at a 2 Hz impact frequency. (c) Linear relationship between the peak current and the relative angle. (d) The coding structure and the anisotropic output signal of the code lock, and the schematic diagram of the signal conversion coding. (e) The arrangement diagram of PVDF ordered fibers in the number "8" and the expression digital signal of the multi-channel synchronous output.

the output digital signal was "3". When the friction angles in the b and e areas were 0°, the output digital signal was "2", when the friction angles of the c and f areas were 0°, the output digital signal was "5". When necessary, a multi-channel reading can be obtained by various traditional electronic devices, making such a design a cost-effective method of anti-counterfeiting.

4. Conclusions

In summary, we report a grating TENG with an anisotropic output. The friction layers were a PVDF fiber array prepared by near-field electrospinning and a PA6 ordered fiber membrane prepared using a parallel electrode collecting device. The short

circuit current and open circuit voltage were 870 nA and 228 V, respectively, and the maximum power density can reach 1800 W m^{-2} through reasonable design methods. The TENG has excellent durability and stability with no significant fluctuations during the 3600 s operating time. The grating TENG can power 230 LEDs and can stably power electronic instruments, calculators, temperature sensors and humidity sensors. By reducing the metal electrode area, the output of the TENG will be increased, which paves a new way for the future design of TENGs with larger outputs. The grating TENG can power LEDs and small devices stably. The TENG has an anisotropic output characteristic, and the output performance can be changed by adjusting the relative orientation of the electrospun nanofiber membrane, which can be used to sense angles or be designed into a self-powered electronic code lock.

Conflicts of interest

There are no conflicts to declare.

Acknowledgements

References

1   Z. L. Wang, On Maxwell's displacement current for energy and sensors: the origin of nanogenerators, *Mater. Today*, 2017, **20**(2), 74–82.

2   Z. L. Wang, J. Chen and L. Lin, Progress in triboelectric nanogenerators as a new energy technology and self-powered sensors, *Energy Environ. Sci.*, 2015, **8**(8), 2250–2282.

3   W. Wang, A. Yu, J. Zhai and Z. L. Wang, Recent progress of functional fiber and textile triboelectric nanogenerators: towards electricity power generation and intelligent sensing, *Adv. Fiber Mater.*, 2021, DOI: 10.1007/s42765-021-00077-9.

4   Z. Li, M. Zhu, Q. Qiu, J. Yu and B. Ding, Multilayered fiber-based triboelectric nanogenerator with high performance for biomechanical energy harvesting, *Nano Energy*, 2018, **53**, 726–733.

5   Z. L. Wang, Triboelectric nanogenerators as new energy technology for self-powered systems and as active mechanical and chemical sensors, *ACS Nano*, 2013, **7**(11), 9533–9557.

6   G. Xiao, J. He, Y. Qiao, F. Wang, Q. Xia, X. Wang, L. Yu, Z. Lu and C.-M. Li, Facile and low-cost fabrication of a thread/paper-based wearable system for simultaneous detection of lactate and pH in human sweat, *Adv. Fiber Mater.*, 2020, **2**(5), 265–278.

7   G. Zhao, Y. Zhang, N. Shi, Z. Liu, X. Zhang, M. Wu, C. Pan, H. Liu, L. Li and Z. L. Wang, Transparent and stretchable triboelectric nanogenerator for self-powered tactile sensing, *Nano Energy*, 2019, **59**, 302–310.

8   X.-X. Wang, N. Wang, H. Qiu, W. Song, Q. Liu, Z. Fan, M. Yu, S. Ramakrishna and Y.-Z. Long, Anisotropic nanogenerator for anticounterfeiting and information encrypted transmission, *Nano Energy*, 2020, **71**, 104572.

9   C. Jiang, C. Wu, X. Li, Y. Yao, L. Lan, F. Zhao, Z. Ye, Y. Ying and J. Ping, All-electrospun flexible triboelectric nanogenerator based on metallic MXene nanosheets, *Nano Energy*, 2019, **59**, 268–276.

10 Q. Ye, Y. Wu, Y. Qi, L. Shi, S. Huang, L. Zhang, M. Li, W. Li, X. Zeng, H. Wo, X. Wang, S. Dong, S. Ramakrishna and J. Luo, Effects of liquid metal particles on performance of triboelectric nanogenerator with electrospun polyacrylonitrile fiber films, *Nano Energy*, 2019, **61**, 381–388.

11 R. Pan, W. Xuan, J. Chen, S. Dong, H. Jin, X. Wang, H. Li and J. Luo, Fully biodegradable triboelectric nanogenerators based on electrospun polylactic acid and nanostructured gelatin films, *Nano Energy*, 2018, **45**, 193–202.

12 J. Wu, W. Liang, W. Song, L. Zhou, X. Wang, S. Ramakrishna and Y. Long, An acid and alkali-resistant triboelectric nanogenerator, *Nanoscale*, 2020, **12**(45), 23225–23233.

13 J. Sun, X. Pu, M. Liu, A. Yu, C. Du, J. Zhai, W. Hu and Z. Wang, Self-healable, stretchable, transparent triboelectric nanogenerators as soft power sources, *ACS Nano*, 2018, **12**(6), 6147–6155.

14 J. Deng, X. Kuang, R. Liu, W. Ding, A. C. Wang, Y. C. Lai, K. Dong, Z. Wen, Y. Wang and L. Wang, Vitrimer elastomer–based jigsaw puzzle–like healable triboelectric nanogenerator for self–powered wearable electronics, *Adv. Mater.*, 2018, **30**(14), 1705918.

15 J. Qian, D.-S. Kim and D.-W. Lee, On-vehicle triboelectric nanogenerator enabled self-powered sensor for tire pressure monitoring, *Nano Energy*, 2018, **49**, 126–136.

16 Z. Ren, Y. Ding, J. Nie, F. Wang, L. Xu, S. Lin, X. Chen and Z. Wang, Environmental energy harvesting adapting to different weather conditions and self-powered vapor sensor based on humidity-responsive triboelectric nanogenerators, *ACS Appl. Mater. Interfaces*, 2019, **11**(6), 6143–6153.

17 Z. Lin, B. Zhang, H. Guo, Z. Wu and Z. L. Wang, Super-robust and frequency-multiplied triboelectric nanogenerator for efficient harvesting water and wind energy, *Nano Energy*, 2019, **64**, 103908.

18 H. Yang, M. Deng, Q. Tang, W. He, C. Hu, Y. Xi, R. Liu and Z. L. Wang, A nonencapsulative pendulum–like paper–based hybrid nanogenerator for energy harvesting, *Adv. Energy Mater.*, 2019, **9**(33), 1901149.

19 H. Wang, Q. Zhu, Z. Ding, Z. Li, H. Zheng, J. Fu, C. Diao, X. Zhang, J. Tian and Y. Zi, A fully-packaged ship-shaped hybrid nanogenerator for blue energy harvesting toward seawater self-desalination and self-powered positioning, *Nano Energy*, 2019, **57**, 616–624.

20 S. Chen, T. Huang, H. Zuo, S. Qian, Y. Guo, L. Sun, D. Lei, Q. Wu, B. Zhu, C. He, X. Mo, E. Jeffries, H. Yu and Z. You, A single integrated 3D-printing process customizes elastic and sustainable triboelectric nanogenerators for wearable electronics, *Adv. Funct. Mater.*, 2018, **28**(46), 1805108.

21 K. H. Ke and C. K. Chung, High–performance Al/PDMS TENG with novel complex morphology of two–height microneedles array for high–sensitivity force–sensor and self–powered application, *Small*, 2020, **16**(35), 2001209.

22 Q. Qiu, M. Zhu, Z. Li, K. Qiu, X. Liu, J. Yu and B. Ding, Highly flexible, breathable, tailorable and washable power generation fabrics for wearable electronics, *Nano Energy*, 2019, **58**, 750–758.

23 H.-J. Qiu, W.-Z. Song, X.-X. Wang, J. Zhang, Z. Fan, M. Yu, S. Ramakrishna and Y.-Z. Long, A calibration-free self-powered sensor for vital sign monitoring and finger tap

communication based on wearable triboelectric nanogenerator, *Nano Energy*, 2019, **58**, 536–542.

24 L. Sun, S. Chen, Y. Guo, J. Song, L. Zhang, L. Xiao, Q. Guan and Z. You, Ionogel-based, highly stretchable, transparent, durable triboelectric nanogenerators for energy harvesting and motion sensing over a wide temperature range, *Nano Energy*, 2019, **63**, 103847.

25 L. Sun, H. Huang, Q. Ding, Y. Guo, W. Sun, Z. Wu, M. Qin, Q. Guan and Z. You, Highly transparent, stretchable, and self-healable ionogel for multifunctional sensors, triboelectric nanogenerator, and wearable fibrous electronics, *Adv. Fiber Mater.*, 2021, DOI: 10.1007/s42765-021-00086-8.

26 S. Wang, L. Lin and Z. L. Wang, Nanoscale triboelectric-effect-enabled energy conversion for sustainably powering portable electronics, *Nano Lett.*, 2012, **12**(12), 6339–6346.

27 G. Zhu, Z. H. Lin, Q. Jing, P. Bai, C. Pan, Y. Yang, Y. Zhou and Z. L. Wang, Toward large-scale energy harvesting by a nanoparticle-enhanced triboelectric nanogenerator, *Nano Lett.*, 2013, **13**(2), 847–853.

28 X. Chen, S. Xu, N. Yao and Y. Shi, 1.6 V nanogenerator for mechanical energy harvesting using PZT nanofibers, *Nano Lett.*, 2010, **10**(6), 2133–2137.

29 L. Gu, N. Cui, L. Cheng, Q. Xu, S. Bai, M. Yuan, W. Wu, J. Liu, Y. Zhao and F. Ma, Flexible fiber nanogenerator with 209 V output voltage directly powers a light-emitting diode, *Nano Lett.*, 2013, **13**(1), 91–94.

30 E. D. Boland, G. E. Wnek, D. G. Simpson, K. J. Pawlowski and G. L. Bowlin, Tailoring tissue engineering scaffolds using electrostatic processing techniques: A study of poly (glycolic acid) electrospinning, *J. Macromol. Sci., Part A*, 2001, **38**(12), 1231–1243.

31 G. Mathew, J. P. Hong, J. M. Rhee, D. J. Leo and C. Nah, Preparation and anisotropic mechanical behavior of highly-oriented electrospun poly(butylene terephthalate) fibers, *J. Appl. Polym. Sci.*, 2010, **101**(3), 2017–2021.

32 A. Theron, E. Zussman and A. L. Yarin, Electrostatic field-assisted alignment of electrospun nanofibres, *Nanotechnology*, 2001, **12**(3), 384.

33 D. M. Rein, Y. Cohen, J. Lipp and E. Zussman, Elaboration of ultra-high molecular weight polyethylene/carbon nanotubes electrospun composite fibers, *Macromol. Mater. Eng.*, 2010, **295**(11), 1003–1008.

34 M. B. Bazbouz and G. K. Stylios, Alignment and optimization of nylon 6 nanofibers by electrospinning, *J. Appl. Polym. Sci.*, 2010, **107**(5), 3023–3032.

35 J. M. Deitzel, J. D. Kleinmeyer, J. K. Hirvonen and N. C. B. Tan, Controlled deposition of electrospun poly (ethylene oxide) fibers, *Polymer*, 2001, **42**(19), 8163–8170.

36 B. Ding, T. Ogawa, J. Kim, K. Fujimoto and S. Shiratori, Fabrication of a super-hydrophobic nanofibrous zinc oxide

film surface by electrospinning, *Thin Solid Films*, 2008, **516**(9), 2495–2501.

37 A. Koski, K. Yim and S. Shivkumar, Effect of molecular weight on fibrous PVA produced by electrospinning, *Mater. Lett.*, 2004, **58**(3–4), 493–497.

38 D. Y. Yang, B. Lu, Y. Zhao and X. Y. Jiang, Fabrication of aligned fibrous arrays by magnetic electrospinning, *Adv. Mater.*, 2007, **19**(21), 3702–3706.

39 D. Sun, C. Chang, S. Li and L. Lin, Near-field electrospinning, *Nano Lett.*, 2006, **6**(4), 839.

40 C. Chang, K. Limkrailassiri and L. Lin, Continuous near-field electrospinning for large area deposition of orderly nanofiber patterns, *Appl. Phys. Lett.*, 2008, **93**(12), 469.

41 D. Li, Y. Wang and Y. Xia, Electrospinning of polymeric and ceramic nanofibers as uniaxially aligned arrays, *Nano Lett.*, 2003, **3**(8), 1167–1171.

42 P. Katta, M. Alessandro, R. D. Ramsier and G. G. Chase, Continuous Electrospinning of Aligned Polymer Nanofibers onto a Wire Drum Collector, *Nano Lett.*, 2004, **4**(11), 2215–2218.

43 H. Laubie, F. Radjai, R. Pellenq and F. J. Ulm, Stress transmission and failure in disordered porous media, *Phys. Rev. Lett.*, 2017, **119**(7), 075501.

44 G. Zhu, Y. S. Zhou, P. Bai, X. S. Meng, Q. Jing, J. Chen and Z. L. Wang, A shape-adaptive thin-film-based approach for 50% high-efficiency energy generation through micro-grating sliding electrification, *Adv. Mater.*, 2014, **26**(23), 3788–3796.

45 J. Henniker, Triboelectricity in polymers, *Nature*, 1962, **196**(4853), 474.

46 D. K. Davies, Charge generation on dielectric surfaces, *J. Phys. D: Appl. Phys.*, 1969, **2**(11), 1533.

47 R. D. I. G. Dharmasena, K. D. G. I. Jayawardena, C. A. Mills, J. H. B. Deane, J. V. Anguita, R. A. Dorey and S. R. P. Silva, Triboelectric nanogenerators: providing a fundamental framework, *Energy Environ. Sci.*, 2017, **10**(8), 1801–1811.

48 J. Shao, M. Willatzen, Y. Shi and Z. L. Wang, 3D mathematical model of contact-separation and single-electrode mode triboelectric nanogenerators, *Nano Energy*, 2019, **60**, 630–640.

49 Z. L. Wang, On the first principle theory of nanogenerators from Maxwell's equations, *Nano Energy*, 2020, **68**, 104272.

50 S. Niu, S. Wang, L. Lin, Y. Liu, Y. S. Zhou, Y. Hu and Z. L. Wang, Theoretical study of contact-mode triboelectric nanogenerators as an effective power source, *Energy Environ. Sci.*, 2013, **6**(12), 3576–3583.

51 Y. Xu, G. Min, N. Gadegaard, R. Dahiya and D. M. Mulvihill, A unified contact force-dependent model for triboelectric nanogenerators accounting for surface roughness, *Nano Energy*, 2020, **76**, 105067.